Journal of Power Sources 207 (2012) 191–198

Contents lists available at SciVerse ScienceDirect

Journal of Power Sources

journal homepage: www.elsevier.com/locate/jpowsour

Redesigning air cathodes for metal–air batteries using MnO_x-functionalized carbon nanofoam architectures☆

Christopher N. Chervin*, Jeffrey W. Long*, Natalie L. Brandell, Jean Marie Wallace[1], Nathan W. Kucko, Debra R. Rolison*

Surface Chemistry Branch, Code 6170, U.S. Naval Research Laboratory, Washington, DC 20375, USA

ARTICLE INFO

Article history:
Received 29 November 2011
Received in revised form 27 January 2012
Accepted 29 January 2012
Available online 5 February 2012

Keywords:
Metal–air
Oxygen reduction
Cathode
MnO_2
Alkaline
Carbon nanofoam

ABSTRACT

We have redesigned the air cathode for metal–air batteries by adapting fiber-paper-supported carbon nanofoams as the base electrode architecture. Electrocatalytic functionality for the oxygen reduction reaction (ORR) is added into the conductive, ultraporous nanofoam paper by electroless deposition at the carbon walls of conformal nanoscopic coatings of birnessite-like manganese oxide (10–20-nm thick MnO_x) via redox reaction with aqueous permanganate (MnO_4^-). We report the ORR activity measured using an air-breathing electroanalytical cell for a series of native and MnO_x-functionalized carbon nanofoams in which the size of the pore network is varied from tens to hundreds of nanometers, the thickness of the air cathode is varied, and the degree of hydrophilicity/hydrophobicity of the electrode structure is altered. Technologically relevant ORR activity is obtained at 0.9 V vs. Zn for MnOx-functionalized carbon nanofoams that are ≥180-μm thick, have pores on the order of 100–200 nm, and are modified with hydrophobic poly(vinylidene difluoride).

1. Introduction

Metal–air batteries rely on gas-phase molecular oxygen as a primary reactant, where the O_2-reduction reaction (ORR) catalyzed within a thin, lightweight "air cathode" charge-balances the oxidation of a bulk metal such as Zn at the anode [1,2]. Zinc–air batteries achieve specific energy in excess of 400 Wh kg^{-1} and 650 Wh L^{-1} in a coin-cell configuration, values that far exceed those of batteries that require two bulk-phase electrodes. The physical structure of the air cathode must support multiple functions—$O_2(g)$ transport, ion transport, electrocatalytic reactivity—functions that currently are adventitiously achieved using "brick-and-mortar" methods to form a powder composite comprising carbon black, catalyst particles (typically manganese oxides), and a hydrophobic polymeric binder [3–5]. Although functional, the ad-hoc distribution of voids within the volume of the typical composite air cathode adversely affects $O_2(g)$ flux and limits the specific power of the metal–air battery.

We have elected to apply an architectural perspective to a redesign of the air cathode, using fiber-supported carbon nanofoam papers as the base electrode platform [6,7]. Carbon nanofoam papers are scalable, device-ready electrode structures that exhibit the following desirable properties: (i) electrical conductivity (10–200 S cm^{-1}); (ii) mechanical integrity; (iii) high specific surface areas (300–500 m^2 g^{-1}); and (iv) through-connected porosity in three dimensions across submillimeter thickness, with the ability to tune the primary pore sizes from nanometers to micrometers [8].

Electrocatalytic functionality is imparted to the carbon nanofoam by incorporating conformal, nanoscale birnessite-like MnO_x coatings (10–20-nm thick) using a simple electroless deposition procedure developed previously for fabricating nanoarchitectured electrodes for electrochemical capacitors [8–10]. This electroless deposition protocol innately electron-wires the otherwise poorly conducting MnO_2 coatings to the massively parallel 3-D current collector (i.e., the carbon nanofoam) thereby obviating the need for additional conductive carbon powder and the polymer binders that are typically required to fabricate powder-composite air cathodes. By using reaction conditions where MnO_2 deposition self-limits, it is possible to preserve the high-quality pore network of the carbon nanofoam, which is critical in maintaining facile O_2 transport throughout the volume of the air cathode.

This new formulation of the air cathode allows us to explore four key parametric variants: (i) pore size (over a range of ~10–200 nm); (ii) electrode thickness (70–230 μm); (iii)

☆ This paper is based on a presentation that was given in the W-Symposium at the EMRS/MRS Meeting in Nice, France, 9–13 May 2011.

* Corresponding authors. Tel.: +1 202 767 0721; fax: +1 202 767 3321.
E-mail addresses: christopher.chervin@nrl.navy.mil (C.N. Chervin), jeffrey.long@nrl.navy.mil (J.W. Long), rolison@nrl.navy.mil (D.R. Rolison).
[1] Onsite contractor with Nova Research Inc., Alexandria, VA 22308, United States.

0378-7753/$ – see front matter © 2012 Elsevier B.V. All rights reserved.
doi:10.1016/j.jpowsour.2012.01.146

the presence or absence of nanoscale MnO_x; and (iv) the importance of the hydrophobic/hydrophilic character of the nanoarchitecture. We find that ORR activity in a three-electrode air-breathing configuration improves when the nanoarchitectured air cathode contains: (i) a pore network of small macropores (50–200 nm); (ii) a thickness greater than 180 μm; (iii) carbon walls that are painted with a nanoscale MnO_x electrocatalyst; and (iv) a hydrophobic coating (poly(vinylidene difluoride), PVdF) that is applied to the outer boundary of the nanofoam electrode.

2. Experimental

2.1. Synthesis of carbon nanofoam papers

Carbon nanofoam papers with pore sizes ranging from 10s to 100s of nanometers and at a nominal thickness of 90, 180, or 270 μm were synthesized using an adaptation of our reported protocol [8] by infiltrating a commercial carbon fiber paper with an aqueous resorcinol–formaldehyde (RF) sol followed by pressure cooking, ambient-pressure drying, and pyrolysis. All reagents were purchased from Aldrich and used without further purification; all aqueous solutions were prepared with 18 MΩ cm H_2O.

To prepare the RF sol, resorcinol, formaldehyde, and water were added to a glass jar with stirring followed by the addition of a catalyst (sodium carbonate). The jar was sealed tightly; the solution was stirred for 30 min and then allowed to oligomerize at room temperature for 3 h. The weight percentage of solids in the precursor sol (wt% RF) and the resorcinol-to-catalyst molar ratio (R/C) were varied by adjusting the quantity of water and the amount of catalyst while maintaining a molar ratio of 1R:2F (resorcinol:formaldehyde). For example, to produce a 40 wt% RF (1500 R/C) sol, one uses resorcinol (10 g; 0.0908 mol), water (10.89 g; 0.604 mol), 37% formaldehyde (14.74 g; 0.1816 mol) and 3 mL of a 20 mM stock solution of sodium carbonate (6.36 mg; 0.06 mmol) (*Caution*: formaldehyde is a possible carcinogen, so minimizing skin contact and inhalation exposure is desirable).

Plasma-etched commercial Lydall carbon fiber papers (stacked for one– through three-layer construction to produce nanofoam papers that were 90-, 180-, or 270-μm thick) were vacuum-infiltrated with the oligomerized RF sol, sealed in a glass-slide assembly with duct-tape and wrapped in aluminum foil. The sealed packets were cured overnight at room temperature and then placed in a consumer-grade pressure cooker (Nesco 3-in-1 pressure cooker) on a slow cook setting (88–94 °C) for 9.5 h, followed by a warming cycle (80 °C) for ~15 h. The RF nanofoam papers were removed from their packets, submerged in water, rinsed with acetone for ~2 h, and then air dried. The resulting RF polymer nanofoam papers were pyrolyzed under argon at 1000 °C for 2 h using a 1 °C min^{-1} ramp to produce conductive, free-standing carbon nanofoam papers.

To produce three distinct pore-size distributions, we synthesized two-layer carbon nanofoam papers using three RF formulations designated as 40/1500 (40 wt% RF (1500 R/C)); 50/1500 (50 wt% RF (1500 R/C)); and 40/500 (40 wt% RF (500 R/C)), respectively. Additionally, the 40/500 formulation was used to infiltrate one-, two-, and three-layer fiber-paper supports to fabricate nominally 90-, 180-, and 270-μm thick nanofoam papers, respectively.

2.2. Functionalization of carbon nanofoam papers with MnO_x and PVdF

Carbon nanofoam papers were modified with nanoscale, birnessite-like MnO_x via electroless deposition from an aqueous $NaMnO_4$ solution [9,10]. Briefly, the carbon nanofoams were infiltrated with 0.1 M Na_2SO_4 under vacuum for 1 h to wet the interior pore walls of the hydrophobic nanofoam paper followed by vacuum infiltration of 0.1 M $NaMnO_4$ in 0.1 M Na_2SO_4 and soaking for 1 h. The MnO_x-modified nanofoam papers were removed from solution and rinsed copiously, followed by soaking in H_2O for 1.5 h, exchanging every 30 min. The modified papers were dried at 50 °C under flowing nitrogen overnight followed by heating to 120 °C in air for 4 h. Selected MnO_x-modified nanofoams were further functionalized with a hydrophobic polymer by vacuum infiltrating with a 3% solution of poly(vinylidene difluoride) (PVdF; Kynar HSV900) in *N*-methyl-2-pyrrolidone (NMP) and soaking for ~12 h followed by blot-drying. The polymer-modified nanofoams were then dried under N_2 at ~50 °C for 12 h.

2.3. Physical characterization of nanofoam papers

The weight loadings of MnO_x in selected functionalized carbon nanofoam papers were determined by ICP-AES (Galbraith, Inc.); the weight loadings of PVdF on the hydrophobized nanofoams were determined gravimetrically by measuring the mass of the paper before and after deposition of PVdF with a microbalance (±8 μg). The morphology of the carbon nanofoam papers before and after functionalization with MnO_x and PVdF were examined by scanning electron microscopy (SEM; Carl Zeiss Supra 55 electron microscope). The specimens were prepared by attaching small portions of the nanofoams to aluminum stubs using carbon tape. The pore–solid architectures of selected nanofoams were characterized with N_2-sorption porosimetry using a Micromeritics ASAP2010 analyzer. Samples were degassed at 120 °C under vacuum for at least 24 h prior to analysis and the pore-size distributions were calculated from the adsorption isotherm and fitted using a density functional theory (DFT) model for a cylindrical geometry and Halsey curve thickness.

2.4. Assembly of an air-breathing three-electrode cell

The O_2-reduction activity of carbon nanofoam-based electrodes was characterized with an in-house-designed air-cathode cell [6] that mimics cathode operation in an alkaline metal–air battery (see diagram in Supporting information, Fig. S1), but incorporates an independent reference electrode [6,11]. The cell was assembled by first attaching a nanofoam (~8 mm × 8 mm) to a Ni-foil flag current collector (perforated with a 6.2-mm hole in the center) using carbon epoxy (DAG EB-020A, Acheson Coatings) such that the perforation was completely covered by the nanofoam. The carbon nanofoam–Ni-flag composite was heated at 170 °C for 5 min to cure the carbon epoxy. A bead of epoxy (Loctite, Hysol) was placed along the outer edge of the nanofoam to provide additional mechanical integrity to the attachment of the nanofoam to the Ni flag. Viton O-rings were aligned around the cut-outs of the nanofoam–Ni-flag composite and sandwiched between two polycarbonate plates (Lexicon 9034 standard) with comparably sized perforations, aligning all cut-out sections. The entire nanofoam–Ni-flag–polycarbonate assembly was affixed by four screws set at the corners of the polycarbonate plates outside of the Ni flag. This cell assembly was then sandwiched between two glass compartments fitted with Viton O-rings. One compartment of the cell was exposed to either ambient air or flowing argon; the other compartment was filled with an alkaline gel electrolyte, taking care to ensure that the gel electrolyte completely filled in the gap created by the O-ring between the nanofoam–Ni-flag assembly and the polycarbonate plate, thus making full contact with the carbon nanofoam electrode surface. External electrical contact was made to the nanofoam via a tab on the Ni flag that extended beyond the dimension of the polycarbonate plates.

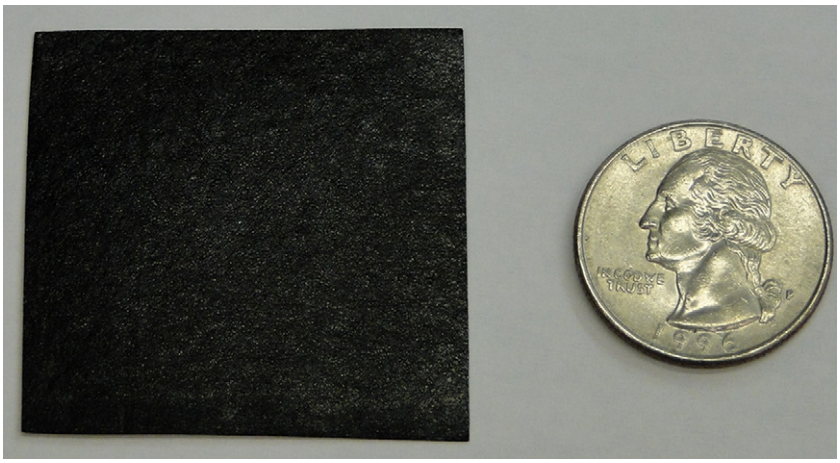

Fig. 1. Optical image of an ~180-μm thick (2-ply), 25 cm^2 40/500 carbon nanofoam paper.

2.5. Electrochemical characterization of carbon nanofoams

The alkaline gel electrolyte was prepared by vigorously blending 12 g of 750 kDa poly(acrylic acid), PAA, in 200 mL of 6 M KOH with a consumer-grade immersion blender until a viscous, translucent gel was formed. Electrochemical measurements were made in the air-cathode cell using a Zn-wire reference electrode (independently measured as 1.44 V vs. Hg/HgO, 1 M KOH) and a platinum-mesh counter electrode immersed in the alkaline electrolyte. Cyclic voltammetric and chronoamperometric measurements were made with the cathode first exposed to argon and then to air. For chronoamperometric measurements, the potential was stepped from 1.425 to 0.900 V vs. Zn, and held for 20 min at each potential with the steady-state current determined once the capacitive currents of the electrode had decayed. The cyclic voltammograms were collected between 1.4 and 0.9 V vs. Zn at 5 mV s^{-1}; the fifth cycle in argon and the second cycle in air are presented in this study. The area of the electrode was taken as the area of the perforation cut into the Ni foil (0.26 cm^2), which is the facial area of the carbon nanofoam electrode exposed to the electrolyte; the total mass of the nanofoam electrode before attaching to the Ni flag was used to normalize the measured capacitance. For comparison, a MnO_x-containing commercial air cathode (E-4 cathode; Electric Fuel) was tested in the air-breathing cell using the same assembly and testing procedure developed for the nanofoam-based air cathodes.

3. Results and discussion

3.1. Characterization of modified and native carbon nanofoam papers

We chose carbon fiber paper as the molding form to fabricate the carbon nanofoams because paper provides desirable, practical features: a binder-free, device-ready structure and a macroscopic form-factor that can be readily scaled in *x* and *y* to establish the geometric footprint and in *z* to vary thickness by stacking multiple layers (ply) of paper (see Fig. 1). In addition to the ability to scale to macroscopic dimensions, the porosity of the nanofoam is easily tuned during synthesis for mesopores (5–50 nm), small macropores (50–200 nm), or large macropores (>500 nm) by adjusting the resorcinol–formaldehyde formulation [8]. These size regimes provide sufficient headspace for further modification of the nanofoam papers with electrocatalytic functionality (e.g., MnO_x or metal nanoparticles) without occluding the open pore network that is needed in rate-critical electrochemical applications [12–14].

The scanning electron micrographs, shown in Fig. 2, give testimony to the dramatic variation of pore–solid architectures that is obtained for the carbon nanofoam papers by adjusting the weight fraction of solids (wt% RF) and the resorcinol-to-catalyst molar ratio (R/C) in the precursor RF sol. Three distinct pore-size distributions were fabricated for this study: small macropores; mesopores; and a mixed distribution of both mesopores and macropores by using RF formulations designated as 40/1500 (40 wt% RF (1500R/C)); 50/1500 (50 wt% RF (1500R/C)); and 40/500 (40 wt% RF (500R/C)), respectively. The porosity retains registry between one-, two-, and three-ply nanofoam papers with the pores open and interconnected in 3D; typically the surface pores, shown in Fig. 2, are slightly larger than pores found within the interior, as we previously reported [8].

Nitrogen-sorption porosimetry, a technique that characterizes pore-sizes below ~100 nm, was used to quantify the bulk mesopore-to-small-macropore-size distribution for the three carbon nanofoam architectures. The pore-size distribution plots are shown in Fig. 2d and the BJH (Barrett–Joyner–Halenda) pore volumes and BET (Brunauer–Emmett–Teller) surface areas that were determined from the porosimetry measurements are listed in Table 1. Although N_2-sorption does not provide a complete description of the larger pores found in the 40 wt% RF nanofoams (see SEM micrographs in Fig. 2), it establishes that there are clear differences between the three nanofoam papers. The porosimetry results are consistent with the microscopy data and show that the 50/1500 nanofoam is mesoporous with an average pore size of 40 nm distributed from 5 to 80 nm, whereas the macroporous 40/1500 nanofoam has little of its pore volume represented by pores smaller than 100 nm and the 40/500 nanofoam has a mixed distribution of both mesopores and macropores ranging from 5 nm

Table 1
Brunauer–Emmett–Teller (BET) surface areas, Barrett–Joyner–Halenda (BJH) pore volumes, and weight percentage MnO_x for two-layer nanofoams.

Sample	BET surface area (m^2 g^{-1})[a]	BJH adsorption pore volume (mL g^{-1})[a]	wt% MnO_x[c]
50/1500	465	0.97	–
MnO_x–50/1500	330	0.44	22
40/500	460	1.3	–
MnO_x–40/500	375	1.1	20
40/1500	345	2.2[b]	–
MnO_x–40/1500	320	Undetermined	7.4

[a] Values are ±2% for replicate analyses within batch and ±10% for batch-to-batch analyses.
[b] Value derived from mercury porosimetry [8].
[c] Values determined by ICP-AES analysis.

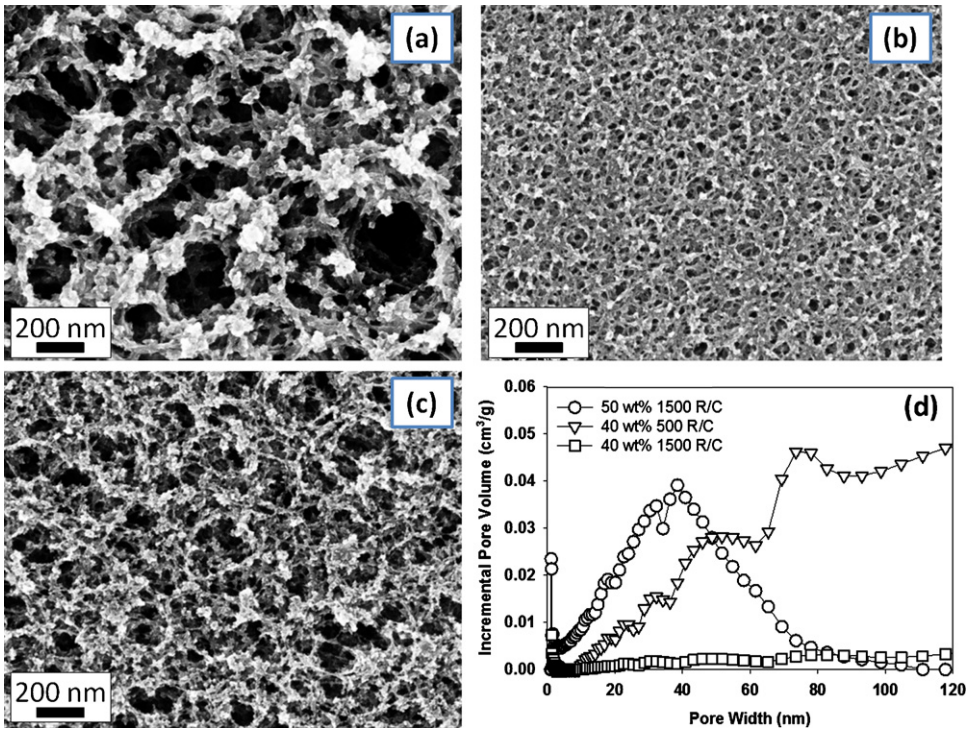

Fig. 2. Scanning electron micrographs of carbon nanofoam papers synthesized with varied weight fraction of solids (40 or 50 wt% RF) and resorcinol-to-catalyst molar ratios (R/C) in order to shift the resulting pore-size distribution: (a) 40/1500, (b) 50/1500, and (c) 40/500; (d) pore-size distribution plots derived from N_2-sorption porosimetry corresponding to the carbon nanofoams in (a) – (c).

to >100 nm. We previously showed using Hg-intrusion porosimetry [8] that the pore sizes of the 40/1500 nanofoam range from 100 to 200 nm. We did not characterize the larger macropores of the 40/500 nanofoam for this study, but on the basis of the micrographic data, some of the pore volume is indeed contained within pores larger than 100 nm. The BET surface areas were 465, 460, and 345 $m^2\,g^{-1}$ for the 50/1500, 40/500, and 40/1500 nanofoams, respectively (see Table 1).

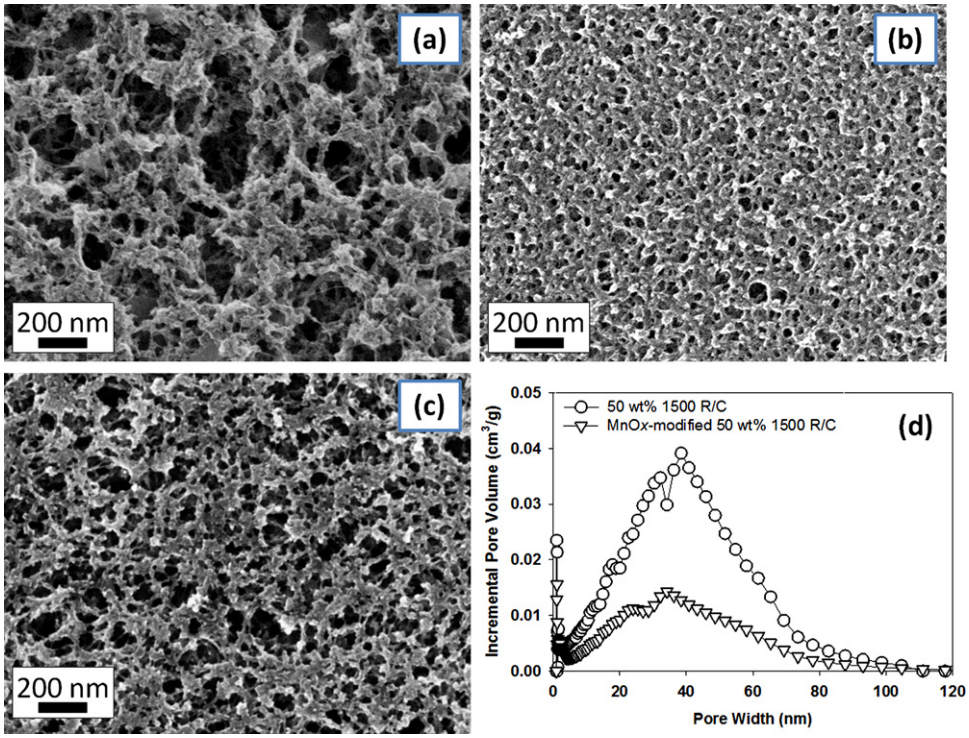

Fig. 3. Scanning electron micrographs of MnO_x-modified carbon nanofoams synthesized with weight fraction of solids (40 or 50 wt% RF) and resorcinol-to-catalyst molar ratio (R/C) of (a) 40/1500, (b) 50/1500, and (c) 40/500; (d) representative pore-size distribution plots derived from N_2-sorption porosimetry for native and MnO_x-modified 50/1500 nanofoams.

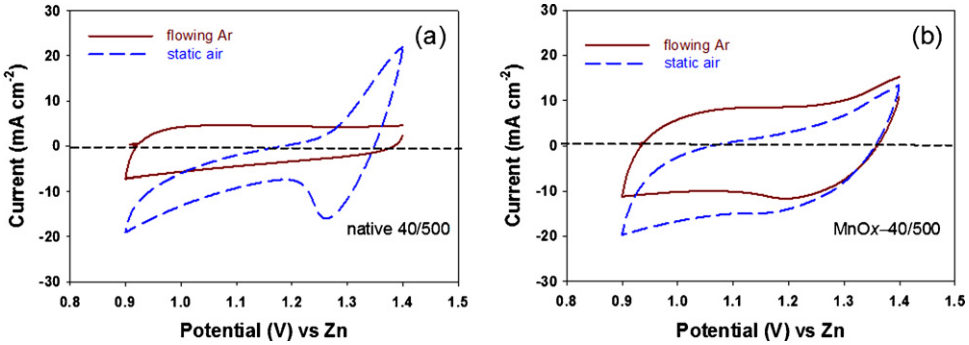

Fig. 4. Cyclic voltammograms in 6 M KOH/PAA electrolyte at 5 mV s^{-1} in (—) argon flow and (– – –) static air of (a) 40/500 carbon nanofoam and (b) MnO_x–40/500 carbon nanofoam. The electrode geometric area is defined as the area of the circular hole cut in the nickel-foil current collector.

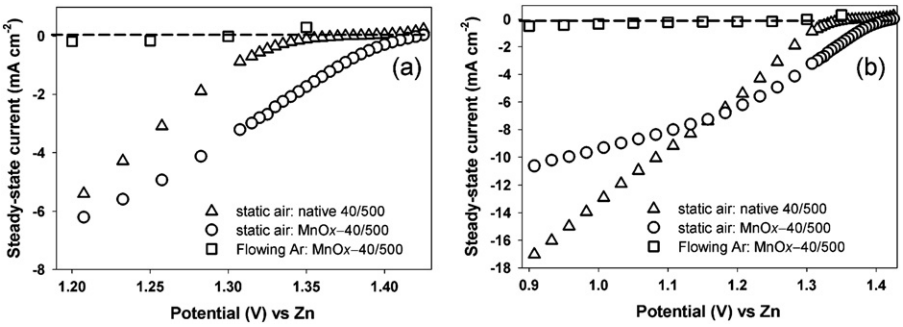

Fig. 5. The current–potential responses in 6 M KOH/PAA electrolyte over (a) the onset potential region and (b) the entire potential window for MnO_x-modified 40/500 carbon nanofoams in (○) air and (□) argon and for a native 40/500 carbon nanofoam in (Δ) air. The steady-state currents were taken after 20 min after each potential step (stepping from 1.425 to 0.9 V vs. Zn). The electrode geometric area is defined as the area of the circular hole cut in the nickel foil current collector.

To incorporate ORR electrocatalytic functionality into the carbon nanofoam papers, we deposited MnO_x coatings (10–20-nm thick) via the self-limiting redox reaction of aqueous permanganate (MnO_4^-) at the exterior and interior carbon surfaces [9,10]; modification of carbon powders and nanostructures by permanganate has also been used to catalyze ORR in powder composite air cathode structures [4,15,16]. The scanning electron micrographs of MnO_x-modified nanofoams demonstrate that the width of the pore network narrows, the MnO_x forms a nanoscale, conformal coating, and the open pore network is not occluded (compare Fig. 3 to the corresponding micrographs of native carbon nanofoams shown in Fig. 2). Nitrogen-sorption porosimetry confirms that the pore structure of the native carbon nanofoam is retained after MnO_x deposition (Figs. 3d vs. 2d and S2), but with a decrease in cumulative pore volume (Table 1), particularly for nanofoams containing smaller pores. Elemental mapping by energy-dispersive spectroscopy of MnO_x-painted carbon nanofoam papers demonstrates that MnO_x is distributed homogeneously throughout the exterior and interior of the paper [9,10] (as seen for the surface of papers in this study, Fig. S3).

The weight loading of MnO_x on the carbon nanofoam papers is controlled by the time of contact with the MnO_4^- solution, the solution concentration, and—because the MnO_x deposits in a conformal fashion without filling the open pores—the substrate surface area. The formulations that generate higher specific surface area accommodate higher loadings of MnO_x: 20 and 22 wt% MnO_x for the 40/500 and 50/1500 two-ply nanofoam papers, respectively, vs. 7.4 wt% MnO_x for the 40/1500 nanofoam with ~25% lower surface area. The one-, two-, and three-layer 40/500 nanofoams had MnO_x loadings of 21, 20, and 17 wt%, respectively; with a typical 10% batch-to-batch variation, these weight loadings only change slightly with thickness, as previously reported [8], again highlighting the quality of the interconnected pore volume across submillimeter lengths.

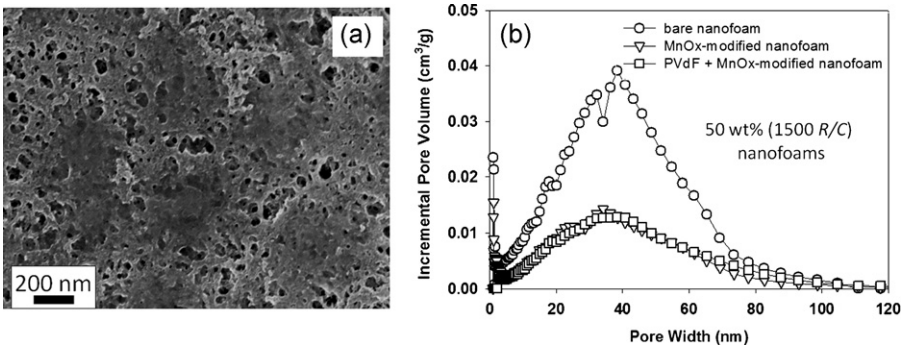

Fig. 6. Scanning electron micrograph of (a) MnO_x–50/1500 carbon nanofoam paper after dip-coating with PVdF; (b) pore-size distribution plots derived from N_2-sorption porosimetry for native, MnO_x-modified, and PVdF + MnO_x-modified 50/1500 nanofoams.

3.2. Electrochemical characterization of modified and native carbon nanofoam papers

To assess ORR activity in our re-designed air-breathing electrode it is important to minimize pore-flooding, which limits current density by hindering $O_2(g)$ transport throughout the volume of the porous cathode to the triple-phase boundaries, where O_2 dissolved in the OH^--conducting electrolyte reacts at the MnO_x/carbon electrocatalytic interface. In an optimized air cathode, the quantity of electrolyte is metered such that it infiltrates the pores and contacts the catalytic surfaces without completely flooding the open channels—only the walls are wetted. If an unflooded pore volume is achieved in our redesigned air-cathode nanoarchitecture, one can then more accurately assess the effect of the nature and weight loading of the electrocatalyst, the size and distribution of the pore network, and the macroscale thickness of the air cathode on performance.

The air-breathing electroanalytical cell [6,11], which differs from conventional three-electrode cells in that the cathode is not intentionally flooded with electrolyte, allows us to gauge how ORR activity is affected by the wetting of the internal surfaces and the degree of pore flooding of the nanofoam electrode—processes that are influenced by the hydrophobic/hydrophilic character of the cathode, its pore-size distribution, and the viscosity of the electrolyte. This cell design also permits rapid toggling between air (or O_2) and an inert gas in contact with the open face of the nanofoam cathode. In the absence of oxygen, the voltammetric response of the native carbon nanofoam is rectangular and symmetric, resulting from double-layer charge storage at the surfaces of the porous carbon (see Fig. 4a for the 40/500 nanofoam). The MnO_x-modified analog also displays a similar capacitive response under argon but with a larger magnitude (see Fig. 4b), an effect that can be ascribed to the redox pseudocapacitance of the nanoscopic MnO_x coating [9,10,17], and also to facile wetting of an initially hydrophobic electrode structure made hydrophilic by coating the walls with MnO_x.

When exposed to air, the native carbon nanofoam exhibits additional cathodic current and a redox peak that arises from O_2 reduction (Fig. 4a); an oxidation peak at >1.25 V vs. Zn on the positive-going sweep is ascribed to oxidation of residual peroxide (HO_2^-), the product of the two-electron reduction of O_2 at carbon surfaces in alkaline medium [18,19]. For the more capacitive MnO_x-modified nanofoam, the ORR current is superimposed on the capacitive background in the negative scan (Fig. 4b). The oxidation of HO_2^- is not observed at MnO_x-modified nanofoams, consistent with the known catalytic activity of MnO_x to decompose peroxide intermediates during oxygen reduction in alkaline medium [3,5]. The cyclic voltammograms for 50/1500 and 40/1500 nanofoam papers, before and after electroless deposition of nanoscopic MnO_x, are similar to the data shown in Fig. 4 (see Fig. S4).

In the air-breathing cell, we obtain quantitative steady-state current densities for the carbon nanofoam papers, free of the overwhelming capacitive background, by stepping the potential through the O_2-reduction wave (Fig. 5). Negligible steady-state current is measured under flowing argon, indicating that O_2 reduction is the source of the increased current in static air. The addition of MnO_x at the walls of the carbon nanofoam provides the anticipated catalytic function, as seen by the shift in the onset of cathodic current to more positive potential (i.e., lower overpotential for ORR; see Fig. 5a). The onset potential for cathodic current is 1.41 and 1.35 V vs. Zn at $-0.1\,mA\,cm^{-2}$ for the MnO_x-modified and native nanofoams, respectively; these potentials are consistent with those observed for ORR at carbon and MnO_x-catalyzed carbon surfaces in aqueous alkaline electrolytes [20–22]. The lowered overpotential for ORR at MnO_x-modified nanofoams is independent of the pore-size distribution and the electrode thickness of the catalyzed

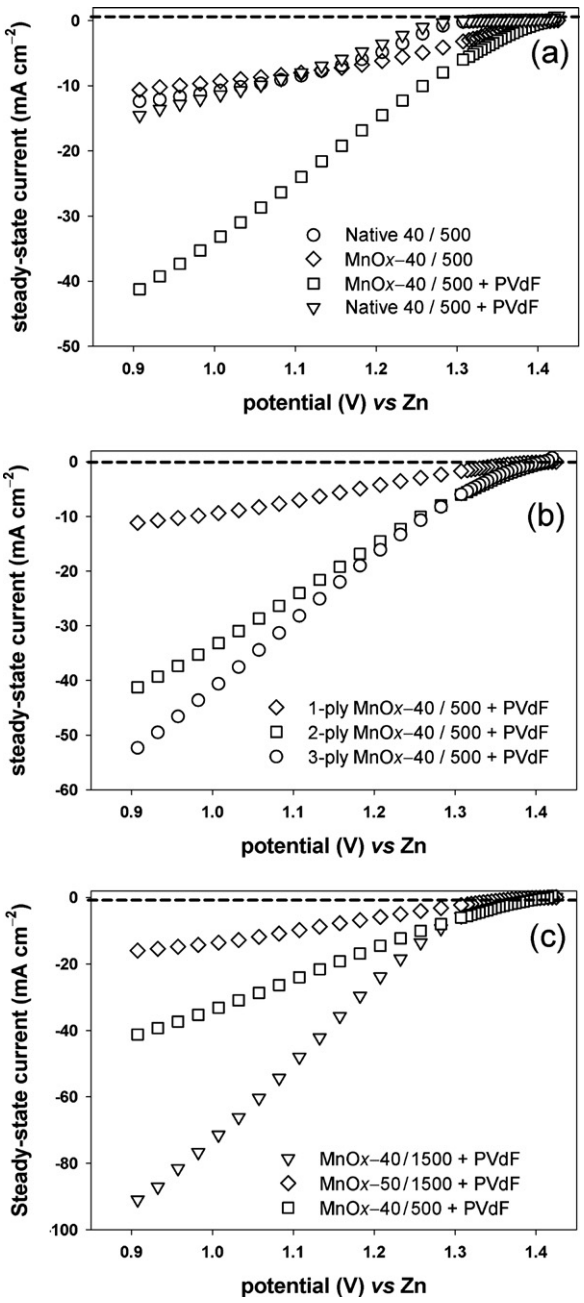

Fig. 7. The effect of adding a hydrophobic component (PVdF) to the nanofoam architecture. Steady-state current densities for (a) 40/500 nanofoam with and without MnO_x and with and without PVdF, (b) one-, two-, and three-ply 40/500 nanofoams after modifying with MnO_x and PVdF and (c) 2-ply nanofoams of different pore structures after modifying with MnO_x and PVdF.

nanofoams (Fig. S5), as expected because the overpotential for ORR depends on the nature of the catalyst and not on the morphology of the electrode.

At high overpotentials for ORR the catalytic benefits of the MnO_x coating are less evident, and the activity of the native carbon nanofoam can even be greater (Fig. 5b). Under such conditions the current density is transport-limited, i.e., controlled by the rate at which O_2 reaches the catalytic surfaces, and thus depends on the extent of electrolyte infiltration, O_2 flux within the volume of the nanofoam, and electrode thickness. We posit that the hydrophilic nature of the MnO_x coating induces electrolyte flooding throughout the nanofoam pore structure, resulting in poor O_2-flux to catalytic

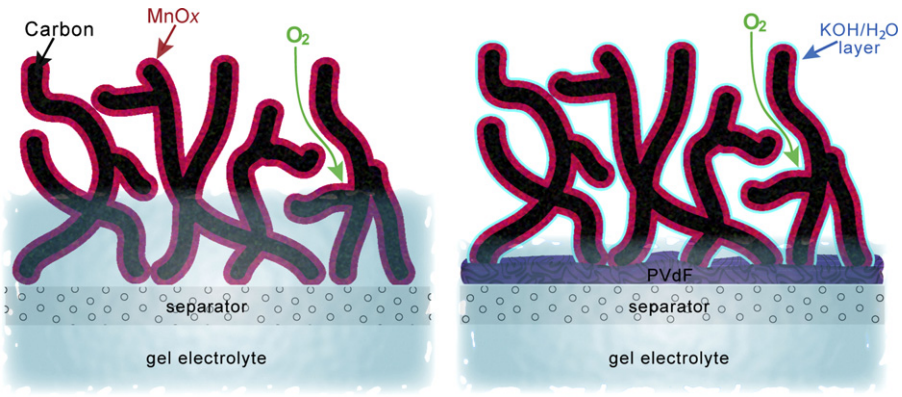

Fig. 8. Cross-sectional schematic of the air/cathode/electrolyte interface without (left) and with (right) the hydrophobic boundary layer.

sites and lower current densities once transport-limited conditions are reached.

3.3. Introducing hydrophobicity to MnO_x-modified carbon nanofoams

Air cathodes should be designed to balance the infiltration of electrolyte pathways to catalytic surfaces with retention of open pore channels to ensure facile gas diffusion within the electrode structure. Conventional air cathodes contain a polymeric additive (e.g., Teflon or PVdF) that both binds together the powder composite and imparts hydrophobic character to the electrode, thereby minimizing electrolyte flooding [23,24]. As a device-ready electrode structure, the MnO_x-painted carbon nanofoam paper has no polymeric binder, thus its surface energy is dominated by the oxide.

We re-introduce hydrophobicity into our binder-free, MnO_x-modified nanofoam papers by simply dipping the paper into a solution of PVdF in NMP. The dip-coated PVdF forms islands on the exterior boundaries of the 40/500 and 50/1500 nanofoams while only partially blocking outer pore mouths (Fig. 6a), whereas for the 40/1500 nanofoam the polymer coats the surfaces of the much larger pores (>100 nm) (Fig. S6). Nitrogen-sorption porosimetry before and after introduction of PVdF indicates that the mesopore/macropore network of the nanofoam is not significantly altered, suggesting that the high molecular weight PVdF coating deposits primarily at the outer boundaries of the nanofoam, with limited intrusion into the bulk volume of the nanofoam paper (Figs. 6b and S7).

Treatment with PVdF dramatically increases the ORR activity of the MnO_x-modified nanofoams (Fig. 7a), with up to four-fold enhancement in current densities at high overpotentials for the 40/500 nanofoam (10 vs. 42 mA cm^{-2} at 0.9 V for native and PVdF-treated MnO_x-modified nanofoams, respectively). The addition of PVdF as a boundary coating likely counteracts the hydrophilic character of the MnO_x coating by providing a balance between sufficient electrolyte wetting of active surfaces vs. flooding the pore structure. As a control experiment, we applied the same PVdF treatment to a representative carbon nanofoam (40/500) with no MnO_x coating. Steady-state measurements under static air showed that the PVdF coating had no significant impact on ORR activity for the native carbon nanofoam electrode (Fig. 7a), which is innately hydrophobic and not likely to experience flooding.

After establishing that the hydrophobic treatment is critical to realize technologically relevant ORR activity, we applied the same PVdF deposition to a series of MnO_x-modified carbon nanofoams in order to systematically examine the effects of electrode thickness and pore-size distribution. Using the 40/500 nanofoam formulation, we determined that the ORR activity increases as we increase nanofoam thickness from one- to two- to three-ply (~90-, 180-, and 270-μm thick, respectively), with the largest jump in activity occurring between one-ply and two-ply (Fig. 7b). When we control electrode flooding with PVdF treatment, thicker electrodes provide a more extended reaction zone per geometric area, which explains the higher observed ORR current density as thickness increases. Ultimately long-range OH^- transport through the electrode volume should limit the extent to which we can achieve gains in ORR activity by increasing thickness. Well-wired ion transport along the walls of the nanofoam could, however, ameliorate even this limitation.

The pore-size distribution of PVdF treated MnO_x-modified nanofoams, which we easily tune during synthesis by adjusting the RF formulation, is critical for ORR activity. We observe higher rates of O_2 reduction for the macroporous 40 wt% RF nanofoams compared to the primarily mesoporous, higher specific surface area 50/1500 nanofoam (Fig. 7c), consistent with the fact that smaller pores should flood more easily via capillary forces. Furthermore, the activity at high overpotential (i.e., high rate) of the relatively mesopore-free 40/1500 nanofoam is >2× that of the mixed meso- and macroporous 40/500 nanofoam (90 vs. 42 mA cm^{-2} at 0.9 V for the 40/1500 and 40/500 nanofoams, respectively) and a >seven-fold increase in activity compared to its PVdF-free MnO_x-modified analog (see Fig. S5). Unlike the macropore-containing nanofoams, which show significant improvement in ORR activity following PVdF modification, the 50/1500 nanofoam has only modestly improved activity compared to its PVdF-free equivalent, suggesting that the small mesopores flood even after the hydrophobic treatment (Fig. S8). Further refinement of the PVdF deposition technique to increase hydrophobicity and prevent flooding of the mesoporous nanofoam architectures should boost their ORR activity by facilitating rapid transport of O_2 through the high-surface-area pore networks that are otherwise flooded.

The O_2-free pseudocapacitance of the MnO_x-modified nanofoams can be used to assess electrochemically active surface area because MnO_x surfaces are only in the circuit to register pseudocapacitance when wetted by electrolyte that is in contact with the bulk electrolyte phase. When expressed in terms of areal (footprint)-normalized capacitance, the voltammograms of untreated and the corresponding PVdF-treated MnO_x-modified nanofoams (40/500 and 40/1500) are nearly indistinguishable (see Fig. S9), indicating that electrolyte pathways permeate the structures to a comparable degree despite the hydrophobic boundary of the PVdF-treated electrodes. The similarity in capacitance contrasts with the four- and seven-fold enhancements in ORR activity when PVdF is present (Figs. 7a and S5), indicating that electroactive surface area is not the limiting factor that establishes ORR activity in the nanofoam-based electrode architecture. Rather, we interpret

these results to indicate that, in the case of PVdF-treated MnO_x-modified nanofoams, a larger fraction of the mesopore/macropore volume remains open, allowing a higher flux of $O_2(g)$ throughout the porous architecture, while the electrode walls are still wetted with electrolyte to provide transport pathways for OH^- generated by O_2 reduction (see schematic in Fig. 8).

4. Conclusions

We have now established the basic design rules for constructing air cathodes based on carbon nanofoam papers: (i) adding the conformal, nanometers-thick, birnessite-like MnO_x coating shifts the onset potential for ORR by >60 mV; (ii) nanofoams with pores in the small macropore range (> 50 nm) outperform those that are primarily mesoporous (< 50 nm) with respect to ORR activity; (iii) thicker nanofoams significantly enhance ORR current densities; and (iv) adding back hydrophobic character to the hydrophilic MnO_x-modified nanofoams is critical to achieve relevant ORR activity. Our preliminary results for ORR activity are competitive with commercially available air cathodes tested in this cell configuration (see Fig. S10) but further refinements in structure and composition are required to realize the performance enhancement that an architectural re-design can provide. We have yet to determine the best blend of pore size and surface area in the nanoarchitecture and the corresponding optimal electrode thickness for that architecture. The degree and dispersal of the hydrophobic component is not optimized. The birnessite-like MnO_x that is produced by the permanganate-based redox deposition is also not the most active polymorph to catalyze O_2 reduction [20,25]. The architectural approach provides additional opportunities to explore: fabricating gradients on both pore size and MnO_x distribution to further enhance molecular and ion transport through the macroscale thickness of the air-cathode architecture.

Acknowledgments

The authors thank Megan B. Sassin for providing the artwork in Fig. 8. Financial support was provided by the U.S. Office of Naval Research.

Appendix A. Supplementary data

Supplementary data associated with this article can be found, in the online version, at doi:10.1016/j.jpowsour.2012.01.146.

References

[1] D. Linden, Handbook of Batteries, 2nd ed., McGraw-Hill, Inc., TX, 1995, pp. 38.1–38.45.
[2] P. Sapkota, H. Kim, J. Ind. Eng. Chem. 15 (2009) 445.
[3] V. Neburchilov, H. Wang, J.J. Martin, W. Qu, J. Power Sources 195 (2010) 1271.
[4] I. Roche, E. Chainet, M. Chatenet, J. Vondrak, J. Phys. Chem. C 111 (2007) 1434.
[5] F.H.B. Lima, M.L. Calegaro, E.A. Ticianelli, Electrochim. Acta 52 (2007) 3732.
[6] J.W. Long, C.N. Chervin, J.M. Wallace, N.L. Brandell, J.L. Dysart, D.R. Rolison, Proceedings of the SPIE Conference on Defense, Sensing, and Security 7679, 2010, pp. 15–21.
[7] C.N. Chervin, J.W. Long, N.L. Brandell, D.R. Rolison, ECS Trans. 35 (33) (2011) 33.
[8] J.C. Lytle, J.M. Wallace, M.B. Sassin, A.J. Barrows, J.W. Long, J.L. Dysart, C.H. Renninger, M.P. Saunders, N.L. Brandell, D.R. Rolison, Energy Environ. Sci. 4 (2011) 1913.
[9] A.E. Fischer, K.A. Pettigrew, D.R. Rolison, R.M. Stroud, J.W. Long, Nano Lett. 7 (2007) 281.
[10] A.E. Fischer, M.P. Saunders, K.A. Pettigrew, D.R. Rolison, J.W. Long, J. Electrochem. Soc. 155 (2008) A246.
[11] Y.L. Cao, H.X. Yang, X.P. Ai, L.F. Xia, J. Electroanal. Chem. 557 (2003) 127.
[12] D.R. Rolison, Science 299 (2003) 1698.
[13] J.W. Long, B. Dunn, D.R. Rolison, H.S. White, Chem. Rev. 104 (2004) 4463.
[14] D.R. Rolison, J.W. Long, J.C. Lytle, A.E. Fischer, C.P. Rhodes, T.M. McEvoy, M.E. Bourg, A.M. Lubers, Chem. Soc. Rev. 38 (2009) 226.
[15] F.P. Hu, X.G. Zhang, F. Xiao, J.L. Zhang, Carbon 43 (2005) 2931.
[16] N. Ominde, N. Bartlett, X.Q. Yang, D. Qu, J. Power Sources 195 (2010) 3984.
[17] J.W. Long, M.B. Sassin, A.E. Fischer, D.R. Rolison, A.N. Mansour, V.S. Johnson, P.E. Stallworth, S.G. Greenbaum, J. Phys. Chem. C 113 (2009) 17595.
[18] P.S.D Brito, C.A.C. Sequeira, J. Power Sources 52 (1994) 1.
[19] I. Morcos, E. Yeager, Electrochim. Acta 15 (1970) 953.
[20] F. Cheng, Y. Su, J. Liang, Z. Tao, J. Chen, Chem. Mater. 22 (2010) 898.
[21] D. Qu, Carbon 45 (2007) 1296.
[22] F.H.B. Lima, M.L. Calegaro, E.A. Ticianelli, J. Eletroanal. Chem. 590 (2006) 152.
[23] M.B. Ji, Z.D. Wei, S.G. Chen, Q. Zhang, Y.Q. Wang, X.Q. Qi, L. Li, Fuel Cells 10 (2010) 289.
[24] Y.G. Wang, L. Cheng, F. Li, H.M. Xiong, Y.Y. Xia, Chem. Mater. 19 (2007) 2095.
[25] W. Xiao, D. Wang, X.W. Lou, J. Phys. Chem. C 114 (2010) 1694.